Hydrogen catalytic performance of hybrid $Fe_3O_4/FeS_2/g\text{-}C_3N_4$ nanocomposite structures

Majed Alshammari[1,*], Sultan Alhassan [1], Khulaif Alshammari[1], Turki Alotaibi [1], Alhulw H. Alshammari[1], Satam Alotibi[2], Taha Abdel Mohaymen Taha[1], Ali Ismael[3]

[1]Physics department, College of Science, Jouf University, P.O. Box: 2014, Sakaka, Saudi Arabia.

2 Department of Physics, College of Science and Humanities in Al-Kharj, Prince Sattam bin Abdulaziz University, Al-Kharj 11942, Saudi Arabia.

[3]Physics Department, Lancaster University, Lancaster, LA1 4YB, UK.

Email address; malshammary@ju.edu.sa

Abstract

In this work, $Fe_3O_4/FeS_2/g\text{-}C_3N_4$ nanocomposites were developed for catalytic hydrogen generation from sodium borohydride. X-ray diffraction (XRD), Fourier transform infrared spectroscopy (FTIR), and environmental scanning electron microscopy (ESEM) were used to analyze these nanocomposites. The XRD diffraction peaks of Fe_3O_4 and FeS_2 cubic phase showed an average crystal size of calculation of 15 and 20 nm. ESEM micrographs showed a 2D broken up sheet structure having more edge sites. The BET surface areas for $S@g\text{-}C_3N_4$, 1.0, 2.0, and 3.0 wt% Fe_3O_4/FeS_2 were 40, 109, 137 and 162 m^2/g, respectively. Even though FeS_2 were incorporated into the nanosheet, the pore size was inccreased from 2.0 to 2.15 nm. $S@g\text{-}C_3N_4$ has an average band gap of 2.60 eV that decreased to 2.30, 2.21 and 2.18 eV at 1.0, 2.0 and 3.0 wt% of FeS_2. In addition, $Fe_3O_4/FeS_2/g\text{-}C_3N_4$ nanosheets showed an emission band at 460 nm. Moreover, the intensity of this band decreased as the content of Fe_3O_4/FeS_2 reached 3.0 wt%. the rate of hydrogen production is accelerated as the percentage of Fe_3O_4/FeS_2 increased from 1.0 - 3.0 wt%. The sample 3.0 wt% Fe_3O_4/FeS_2 showed the best rate of hydrogen production (8480 mL/g.min).

Keywords: $NaBH_4$; Fe_3O_4/FeS_2 nanosheet; Hydrogen production; Methanolysis

1. Introduction

Recently, improving hydrogen production is a research priority in various research sectors. Production improvement includes many means, including the use of catalysts. Therefore, tailoring the catalyst during the preparation process by controlling the shape, size and surface properties is very important to increase performance [1-3]. Nanosheets have achieved great success when used as hydrogen production catalysts. The structural, electrical, and mechanical properties of carbon nitride (g-C_3N_4) have drawn much attention in physicochemical studies [4,5]. Meanwhile, g-C_3N_4 contains carbon and nitrogen that are abundant elements. g-C_3N_4 exhibits a prominent UV-Vis absorption peak in the optical wavelength of 260-320 nm. The absorption peak at around 250 nm is caused by the π - π^* electron transfer for g-C_3N_4 with s-triazine rings. While the absorption band located at 320 nm was formed by the transitions of electrons at n - π^* that include a lone pair of electrons on nitrogen atoms in g-C_3N_4 [6,7]. Moreover, g-C_3N_4 has improved thermal stability for catalytic application because of high strength up to 600 ^oC. However, the electroactive surface area and conductivity of g-C_3N_4 are both low [8-10]. The key factors limiting effectiveness are low carrier mobility and high bulk recombination.

The g-C_3N_4 nanosheet consists of stacked layers, and for this, it needs to be modified with other nanomaterials to improve its catalytic efficiency. This goal can be achieved by grafting them with different minerals, metal oxides, or metal sulfides. This procedure, in turn, will combine the features of g-C_3N_4 nanosheets with these nanomaterials in the final composite. The procedure must take into account the grafting ratios and the morphology of the composite as well as the surface characteristics. As a result, electron-hole recombination is suppressed.

The semiconductor nanoparticles of iron sulfide are naturally abundant and non-toxic and thus have more interest [10-13]. These materials are flexible and can be prepared with different sizes and morphologies. This diverse group of complexes exists in various phases, including greigite, marcasite, pyrrhotite, pyrite and troilite. The energy gap of these materials is 0.8 – 0.95 eV and possess an absorption coefficient of ~10^5 cm^{-1}. The stoichiometric iron sulfide (FeS_2) exhibits antiferromagnetic properties at room temperature [14-16]. The FeS_2 catalyst can act as an electron trap and a site for H_2 production to enhance interfacial charge transfer and separation. For catalytic

applications, nanoscale FeS_2 with an appropriate surface charge and functionality may be of significance. The development of a precise preparation technique is therefore essential to link nickel sulfides with the g-C_3N_4 nanosheet. Iron oxide is a commonly used co-catalyst in photocatalytic reactions due to its ability to enhance charge separation and transfer to improve the performance of the catalyst [17]. Combining iron oxide with carbon nitride catalyst can help to improve the efficiency and effectiveness of the catalyst for various chemical reactions. Iron oxide can act as a co-catalyst and help to promote electron transfer and improve the catalytic activity of carbon nitride. This combination can also increase the stability of the catalyst and enhance its performance in various applications such as water purification, organic synthesis, and energy conversion. Therefore, the nanocomposites of Fe_3O_4/FeS_2/g-C_3N_4 will show high surface area including many catalytic active sites.

Efforts have been made to engineer the structure of carbon nitride by modifying with metals or metal oxides to improve its efficiency as a catalyst. Moreover, the works included other matrices such as graphene and metal organic frameworks (MOF) because of their structural advantages.

Phosphorus was used to modify the surface properties of g-C_3N_4-titanium oxide composites to function as a catalyst for the extraction of hydrogen from sodium borohydride [18]. These composites showed a significant improvement in stimulating hydrogen production, and the value of the production rate was 14750 mL $min^{-1}g^{-1}$. Meanwhile, the activation energy of the hydrogen production process was 36 kJ mol^{-1}. In the previous work, we dealt directly with the preparation of NiS/g-C_3N_4 sheets using the polycondensation method [19]. Hydrogen production measurements were completed from the methanolysis reaction of $NaBH_4$. The study succeeded in achieving a hydrogen production rate of 8654 mL/g.min. Kottaikalai Ganesan et al [20] have conducted a study of phosphorylated silica as a catalyst from $NaBH_4$ methanolysis reaction. The prepared material was incorporated into the hydrogen production process and achieved a rate of 762.4 mL $min^{-1}g^{-1}$. The study completed the calculation of the activation energy for the hydrogen production process and the value was 29.92 kJ mol^{-1}. On the other hand, an experimental study appeared for the preparation of g-C_3N_4/SiO_2/N nanocomposites as a catalyst for hydrogen production [21]. Laboratory measurements of hydrogen production rates in the case of catalyst g-C_3N_4/SiO_2/N showed a value of 11400 mL $min^{-1}g^{-1}$. The activation energy for the self-hydrolysis of $NaBH_4$ was 33.2 kJ mol^{-1}. In another context, the MoO_3/S@g-C_3N_4 nanocomposites were

prepared at different carbon nitride content [22]. The nanocomposite of MoO_3/10wt%S@g-C_3N_4 showed the highest rate of hydrogen production (18421 mL/g·min). Chemical reduction was used to prepare highly distributed CoB alloys imbedded on MOF-74-derived graphene nanosheets [23]. The measurements were conducted on the catalyst in the reaction of methanolysis from $NaBH_4$ and showed a production rate of 7937 mL $min^{-1}g^{-1}$. The activation energy for self-hydrolysis of $NaBH_4$ is calculated to be 38.8 kJ mol^{-1}. To the best of our knowledge, there is no any research investigated the preparation of Fe_3O_4/FeS_2/g-C_3N_4 hybrid catalyst for hydrogen evolution from $NaBH_4$.

In order to increase the catalytic activity of g-C_3N_4, the current work seeks to identify an acceptable precursor, morphology, exfoliation condition, and synthesis techniques for carbon nitride composites. Therefore, Fe_3O_4/FeS_2/g-C_3N_4 sheets were prepared by the direct decomposition/polycondensation of nickel chloride and thiourea at 550 ºC. Various techniques have been used to clarify the structural properties of nanocomposites, such as XRD, FTIR, and ESEM. A surface area analyzer investigated surface properties such as surface area and porosity of nanosheets. Electronic configuration analysis of the prepared samples was completed by optical absorption as well as emission measurements. Moreover, these nanocomposites have been applied as catalysts in hydrogen production processes from methanolysis reaction of $NaBH_4$. All procedures were carried out at room temperature and the amount of hydrogen was determined using the water displacement technique. Interestingly, the nanosheets achieved high hydrogen production rates, especially for the sample with a concentration of 3 wt% Fe_3O_4/FeS_2.

2. Experimental

Iron trichloride hexahydrate ($FeCl_3.6H_2O$, 97%), thiourea ($NH_2.CS.NH_2$, 99%) and sodium borohydride ($NaBH_4$, 97%), were obtained from Loba Chemi, Mumbai, India, and were used without further purification. While, The Sigma-Aldrich, Darmstadt, Germany provided the absolute methanol.

For the synthesis of S@g-C_3N_4, 10.0 g of thiourea were heated in a porcelain crucible in the muffle furnace at 550 °C for 120 min with a heating rate of 3.0 °/min. After cooling to room temperature, the yellow solid mass in the crucible was ground inside an agate mortar. Thereafter, Fe_3O_4/FeS_2/g-C_3N_4 nanocomposites were prepared by grinding 10 g of thiourea and 1.0, 2.0 and 3.0 wt% of

$FeCl_3.6H_2O$ for 30 min. The mixture was then poured into porcelain crucibles that were placed within a muffle furnace and secured with a lid. The polycondensation procedure was completed at 550 ºC for 2 h with a ramping rate of 3.0 ºC/min. After allowing the acquired nanocomposite samples to cool, they were ground.

Structure-related variables including crystal structure, crystal size, and microstrain were examined by X-ray diffraction analyses. The Shimadzu XRD 700 device used a $Cu_{k\alpha}$ wavelength of 1.54056 Å to generate the XRD spectra. The diffraction pattern of the produced nanocomposite was compared to the JCPDS files in the database to determine the crystal structure. A Shimadzu FTIR spectrometer, model 100 Tracer, was used to acquire FTIR measurements. Typically, frequency ranges between 4000 and 399 cm^{-1} were optimized. The energy dispersive X-ray analysis (EDX) accessory, when used in conjunction with the sensitive characterization equipment ESEM, reveals surface morphology and identifies the elemental content of materials. Using a Thermofisher Quattro environmental scanning electron microscope (ESEM), ESEM micrographs and EDX scans were collected. The prepared samples were degassed at 77 K before recording the adsorption-desorption data on the NOVA 4200e surface area analyzer, the samples were exposed to N_2 gas at 77 K. Optical spectroscopy is based on the absorption of photons to excite the electrons from valence to conduction band. The measurements of optical absorption for the nanocomposites were conducted on a Thermo fisher Evo 201 UV-Vis spectrophotometer. The spectra of photoluminescence (PL) were completed at an excitation wavelength of 350 nm on the Cary Eclipse fluorescence spectrometer.

The prepared $Fe_3O_4/FeS_2/g\text{-}C_3N_4$ nanosheets were used as a catalyst for hydrogen production from methanolysis reaction of $NaBH_4$. All hydrogenation tests were conducted in a glass reactor with a 250 mL capacity and a glass stopper for closing. In a typical experiment, the desired amount of catalyst (20 mg) was mixed along with the $NaBH_4$ (25 mg). The mixture was charged into the reactor with 10 mL methanol. Immediately, the self-hydrolysis of $NaBH_4$ started and hydrogen gas released. The reaction was conducted at constant temperature (293 K), and the H_2 volume as a function of time was measured. The water displacement method was applied to measure the volume of H_2 gas. These experiments were repeated 3.0 times with an experimental error of ±5.0%. Finally, All the hydrogen catalytic reactions were performed in the ordinary visible light.

3. Results and discussion

The crystal structure and crystallite size of materials are easily obtained from XRD analysis. Fig. 1 displays the XRD data of the fabricated Fe_3O_4/FeS_2/g-C_3N_4 nanocomposite catalysts. The spectrum of S@g-C_3N_4 nanosheet revealed two major peaks at 13.08° and 27.20°. The minor diffraction peak at 13.08° matches the (100) plane [24,25]. While the intense peak at 27.20° matches the (002) plane that comes from interlayer stacking of g-C_3N_4 structure. Moreover, the (100) plane has been attributed toward the inter-planar configuration of aromatic systems, and the crystal plane (002) to the interlayer construction of aromatic systems [26]. The diffraction peak intensity of the planes (100) and (002) have decreased in Fe_3O_4/FeS_2/g-C_3N_4 composites with different concentration in comparison to S@g-C_3N_4 nanosheet. Whenever compared to the S@g-C_3N_4 peak position of 27.2°, at 3.0 wt.% of Fe_3O_4/FeS_2 shifted to a higher angle of 27.8°. The main reason for this shift is the condensation of carbon nitride or shrinkage of the layer stacking direction [27]. In addition, the thickness of carbon nitride layers is reduced in accordance with the shift of peak position [28].

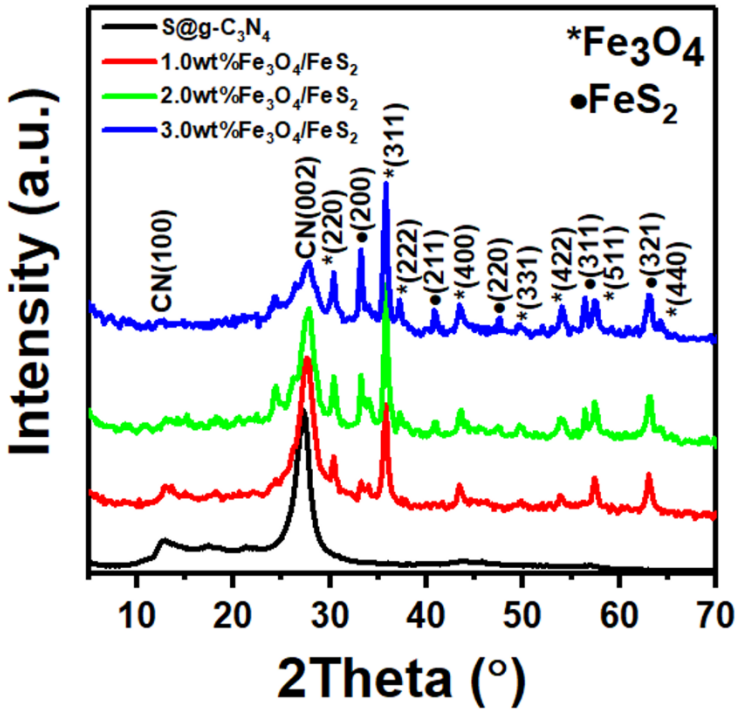

Fig. 1 XRD spectra of Fe_3O_4/FeS_2/g-C_3N_4 nanosheets

The cubic crystal phase of Fe_3O_4 showed diffraction peaks at 30.36, 35.78, 37.20, 43.53, 47.52, 54.02, 57.42 and 63.01°. The reflections of these peaks are (220), (311), (222), (400), (331), (422), (511) and (440), respectively [29]. The diffraction angles 33.2, 40.8, 47.50, 56.39 and 64.19° are related to the FeS_2 reflections (200), (211), (220), (311), and (321), respectively [30]. The broadening of these diffraction peaks nearly the same whatever the content of FeS_2 increased up to 3.0 wt%. Furthermore, the Scherer equation suggests the relationship between the crystallite size (D) and the diffraction peak widening (β) as follows [31-33];

$$D = \frac{0.9\lambda}{\beta \cos\theta} \quad (1)$$

For the diffraction peak (002), the values of β increased upon the increase of FeS_2 wt%. This result is indicative of the small S@g-C_3N_4 crystalline domains. The average crystal size determined by the Scherer equation for Fe_3O_4 and FeS_2 to be 15 and 20 nm. Furthermore, the Fe_3O_4/FeS_2 integration into carbon nitride revealed a shift of (002) peak that indicate the preparation of nanocomposite sheets.

FTIR profiles of Fe_3O_4/FeS_2/g-C_3N_4 nanosheets were collected and displayed in Fig. 2. Analysis of the spectra in the 3100-3300 cm^{-1} region, shows stretching vibrations of N-H and H_2O [34]. The vibrations of C=N bond occur at 2170 cm^{-1} [35]. The peaks in the region 1229-1628 cm^{-1} are assigned to CN heterocycles at stretching modes [36]. The absorption bands detected at 1010 and 1132 cm^{-1} are due to stretching vibrations of C-O and C-OH [37].

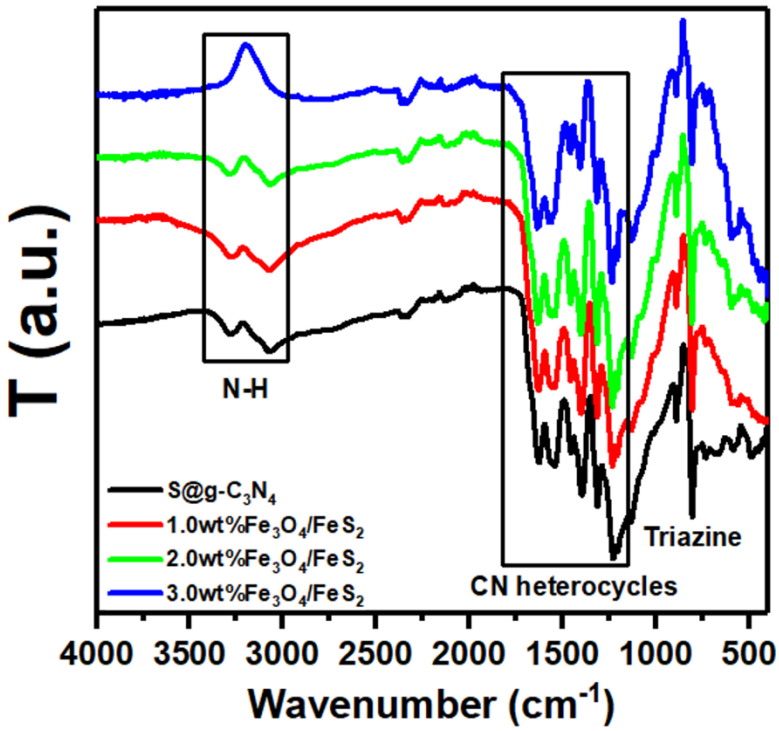

Fig. 2 FTIR spectra of Fe_3O_4/FeS_2/g-C_3N_4 nanosheets

The spectra of all samples reveal a strong band at 804 cm^{-1} for heptazine or triazine blocks [38]. Partly, the bonds of C-N(-C)-C generate the absorption band at 1311 cm^{-1}. Moreover, the C–N (sp^3) bond vibrations show an absorption peak at 1205 cm^{-1} [39]. The varied levels of interlayer FeS_2 may be the cause of the variations in intensities and shifts. These findings support the XRD examinations and show that Fe_3O_4/FeS_2/g-C_3N_4 nanocomposites were successfully synthesized at 550 ºC.

ESEM images were used to examine the shape and structure of the fabricated Fe_3O_4/FeS_2/g-C_3N_4 nanocomposite. The collected micrographs for the powder samples were illustrated in Fig. 3. The image of sulfur/g-C_3N_4 showed a 2D flake morphology. In the case of Fe_3O_4/FeS_2/g-C_3N_4 nanocomposites, sheet materials have been split up throughout the growing process, revealing additional edge sites. The 2D sheet morphology of the Fe_3O_4/FeS_2/g-C_3N_4 nanocomposites support the data analysis of XRD and FTIR. Moreover, the results of ESEM micrographs indicate an increase of surface area as the ratios of FeS reaches 3.0 wt%. The EDS elemental data plotted in Fig. S1 reveal the compositional ratios of C, N, Fe, O and S.

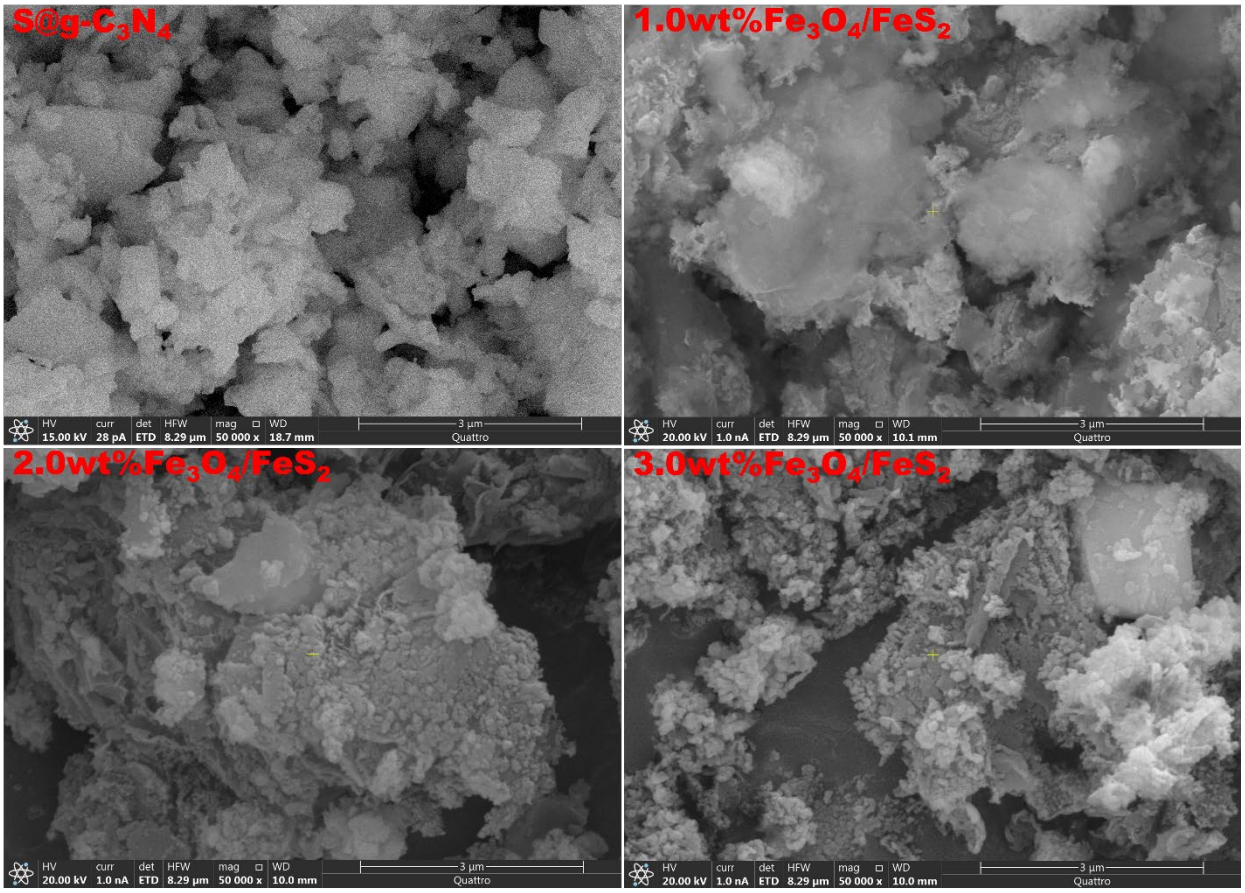

Fig. 3 ESEM images of $Fe_3O_4/FeS_2/g\text{-}C_3N_4$ nanosheets

The study of the surface properties of nanocomposites represents the most important method for determining the initial catalyst efficiency. Therefore, we have measured the adsorption-desorption data of the $FeS_2/g\text{-}C_3N_4$ nanocomposites as shown in Fig. 4. The shape of isotherms agrees with the IV type that corresponds to mesoporous structure. The sample $S@g\text{-}C_3N_4$ showed a surface area BET of 40 m^2/g. Meanwhile, the $Fe_3O_4/FeS_2/g\text{-}C_3N_4$ nanosheets have a surface area of 109, 137 and 162 m^2/g at 1.0, 2.0 and 3.0 wt%. According to these data, the intercalation of Fe_3O_4/FeS_2 into $g\text{-}C_3N_4$ nanosheets increased the surface area and thus increased the number of active sites. Moreover, the BJH model was applied to the collected data to estimate the pore size values. In that case, the pore size for the sample $S@g\text{-}C_3N_4$ was 2.0 nm. While the pore size data for the $Fe_3O_4/FeS_2/g\text{-}C_3N_4$ nanosheets were 1.55, 1.77 and 2.15 nm at 1.0, 2.0 and 3.0 wt%. Indeed, the sample 3.0 wt% of Fe_3O_4/FeS_2 has the highest surface area and pore size. Therefore, this sample may possess the highest catalytic performance to produce hydrogen.

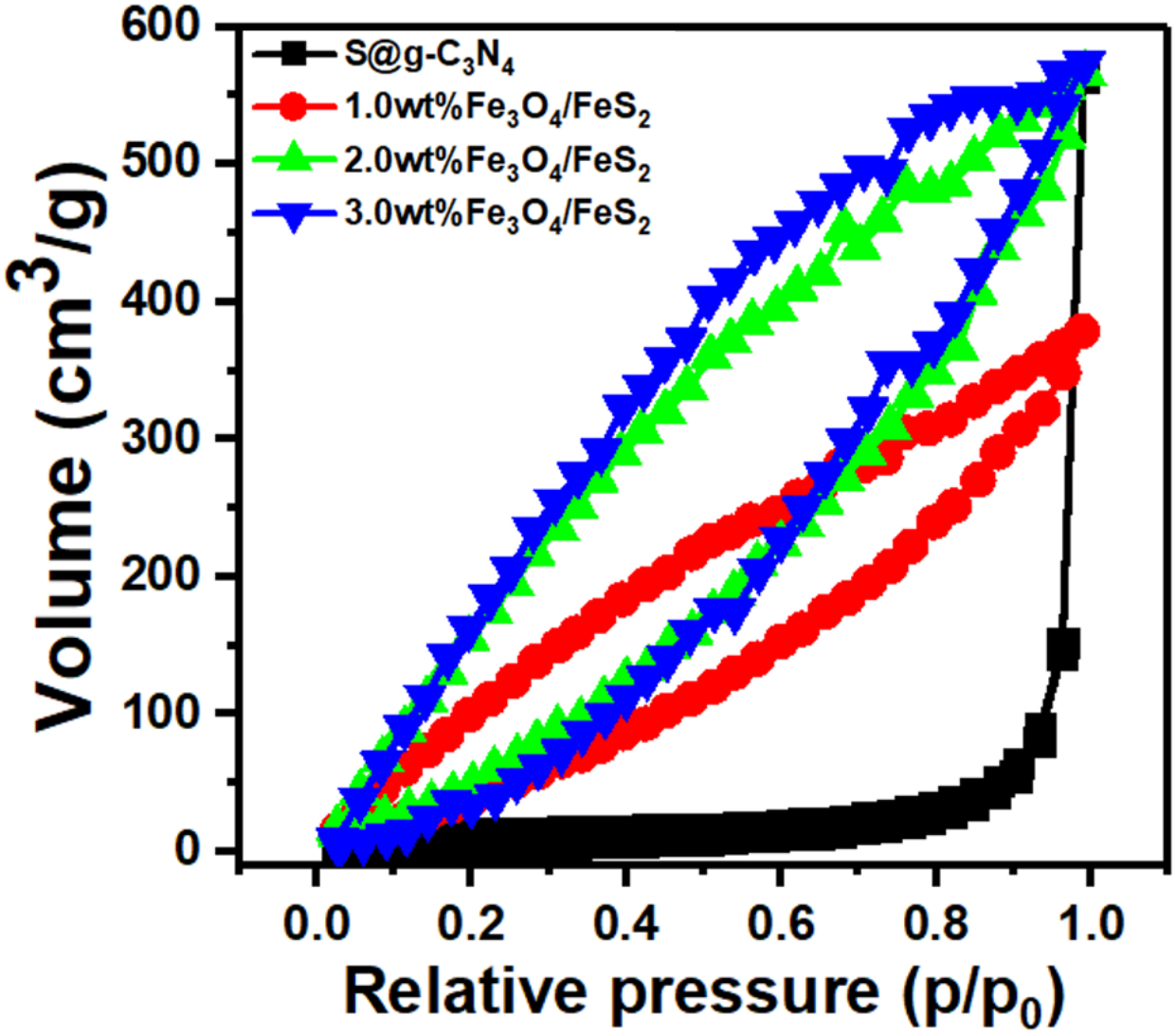

Fig. 4 N_2 isotherm data of $Fe_3O_4/FeS_2/g\text{-}C_3N_4$ nanosheets

The optical properties, such as absorbance and the optical band gap of nanocomposites were studied as follows. The absorbance parameters were measured by UV–Vis spectroscopy, as shown in Fig. 5a. The wavelength ranges are about 200 to 1000 nm. The absorbance peak is appeared at around 320 nm corresponding to n → π^* electronic transitions [40]. The peaks of absorbance are red shift due to generating photo-induced electrons and holes. The absorption band tail corresponding to heterocyclic aromatics π-π* transitions appeared around 400 nm [41].

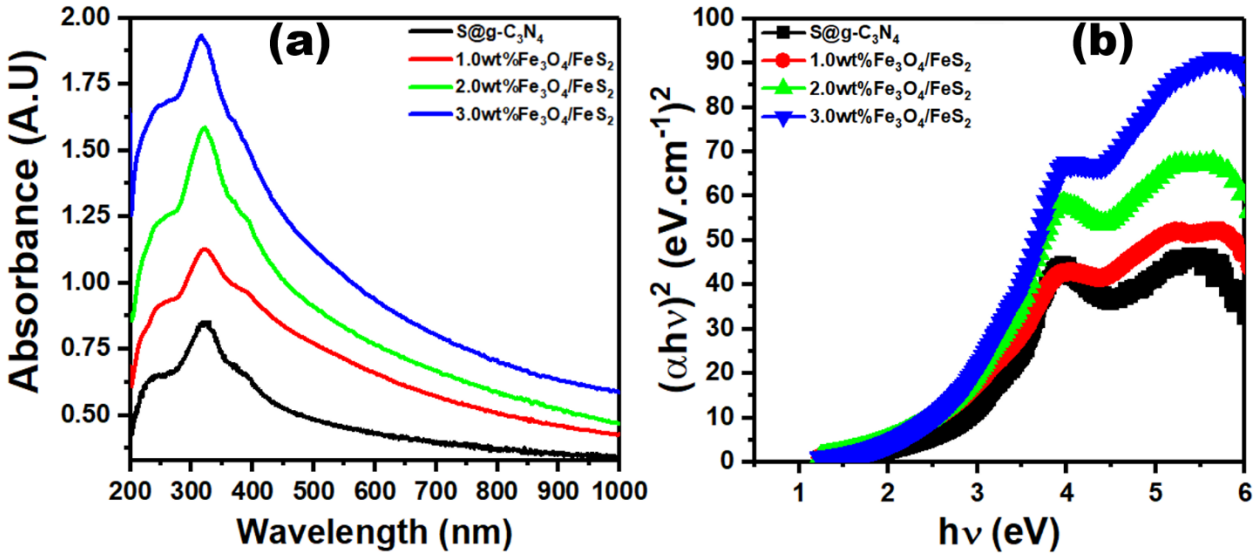

Fig. 6 Graphs of (a) absorbance vs wavelength and (b) $(\alpha h\nu)^2$ vs hν for $Fe_3O_4/FeS_2/g\text{-}C_3N_4$ nanosheets

The study of the optical energy gap (E_{opt}) of nanocomposites represents the most important method for determining the electronic structure of a catalyst. For that reason, the equation proposed by Tauc was applied to estimate the optical band gap values [42-44];

$$\alpha h\upsilon = k(h\upsilon - E_{opt})^{0.5} \qquad (2)$$

The optical band gaps (E_{opt}) can be determined from Fig. 5b. The values of the E_{opt} are estimated by the straight-line intercept from the $(\alpha h\nu)^2$ against hν. The values are 2.60, 2.30, 2.21 and 2.18 eV for ($S/g\text{-}C_3N_4$), (1 wt% of $Fe_3O_4/FeS_2/g\text{-}C_3N_4$), (2 wt% of $Fe_3O_4/FeS_2/g\text{-}C_3N_4$), and (3 wt% of $Fe_3O_4/FeS_2/g\text{-}C_3N_4$), respectively. These values decrease as the concentration increase; possibly due to the development of energy levels [45].

When the materials are pumped with photon energy, many electron-hole pairs generated at the excited energy states. In that case, the induced electron hole pairs remain for a lifetime and then recombine. The photoluminescence spectra of the prepared $Fe_3O_4/FeS_2/g\text{-}C_3N_4$ nanosheets are plotted in Fig. 6. From inspection of this figure, all the samples show an emission peak around 460 nm that related to the transitions of n-π* [46]. However, the increase of Fe_3O_4/FeS_2 percentage reduced the intensity of this peak. This decrease is explained by the delay in the recombination of the electrons and holes [47]. For that reason, the catalytic performance of the $Fe_3O_4/FeS_2/g\text{-}C_3N_4$ nanosheets may be improved.

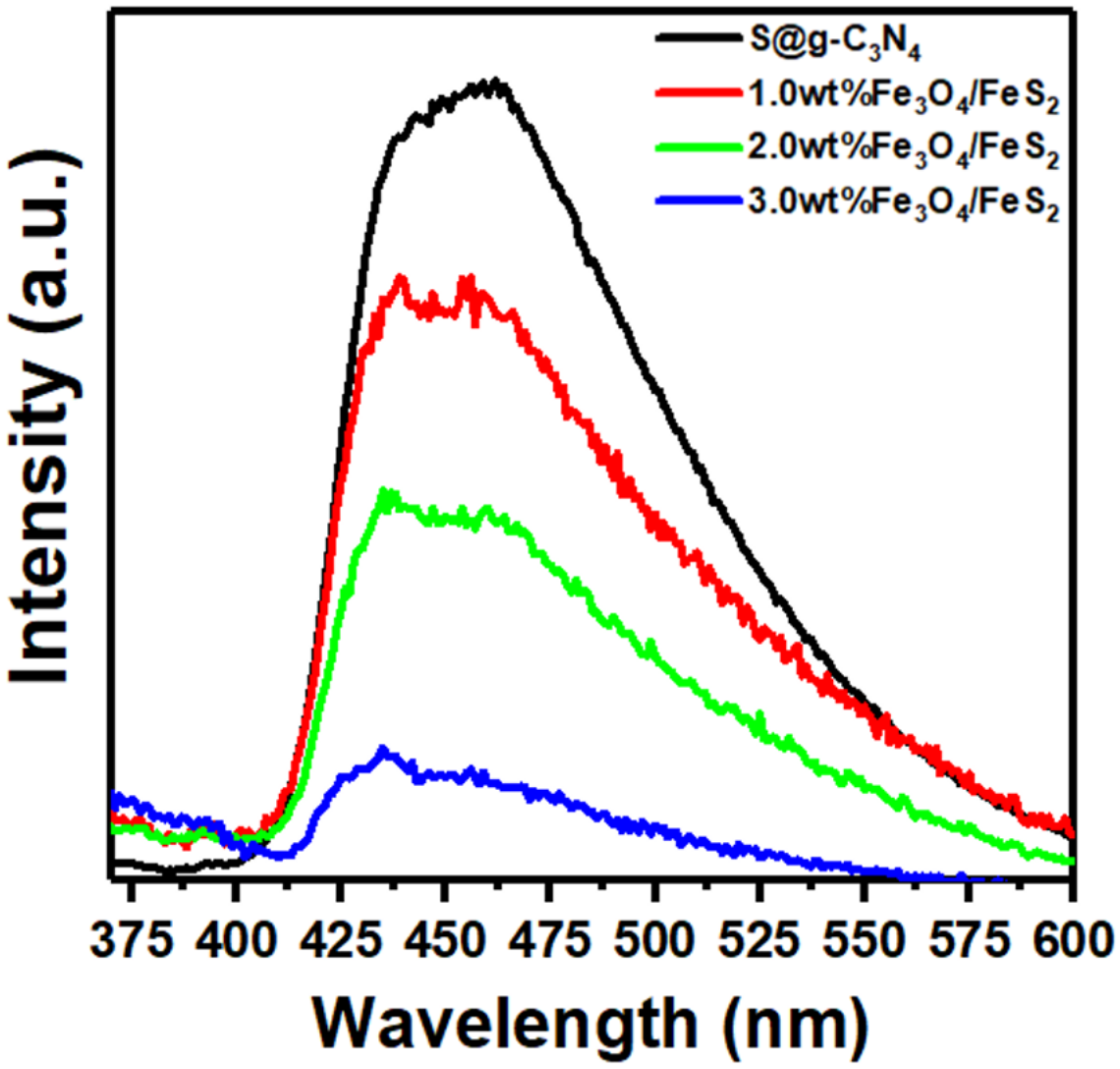

Fig. 6 Emission spectra of $Fe_3O_4/FeS_2/g\text{-}C_3N_4$ nanosheets

The method of self-decomposition of sodium borohydride in a methanol solution occupies a great deal of interest because it has high stability and provides a low temperature. Moreover, this mechanism produces hydrogen gas rapidly and with high rates [48]. Therefore, this reaction was used to test the efficiency of $Fe_3O_4/FeS_2/g\text{-}C_3N_4$ nanocomposites as a catalyst for hydrogen emission from $NaBH_4$. Firstly, the volume of H_2 gas was recorded at various times at 293 K. Fig. 7 display the curves of hydrogen volume at different times for the $Fe_3O_4/FeS_2/g\text{-}C_3N_4$ nanosheets.

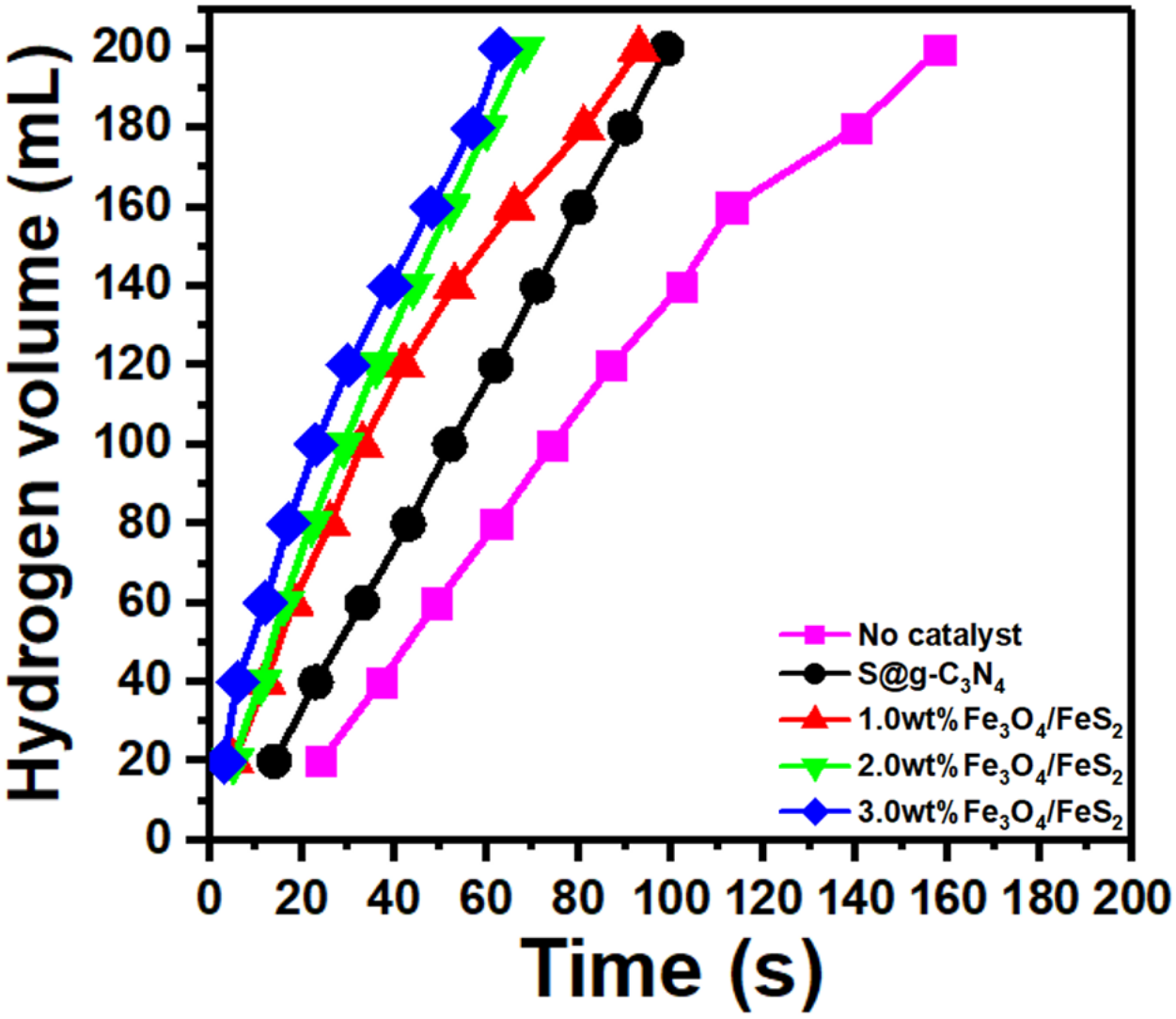

Fig. 7 H_2 volume vs time at 20 mg of $Fe_3O_4/FeS_2/g\text{-}C_3N_4$ catalyst and 2.5% $NaBH_4$

Fig. 7 indicates that the rate of hydrogen production is enhanced as the percentage of Fe_3O_4/FeS_2 increased. This comes due to the improvement of surface area and pore size that contained more catalytic active sites. In considering the decomposition of $NaBH_4$ in methanol solution, two ions are produced Na^+ and BH_4^- [49]. The catalyst's surface may adsorb BH_4^- and CH_3OH molecules from the solution. A new electron is added to the hydrogen atom in its hydridic form (H^-), while the BH_3^- species is still bound to the $Fe_3O_4/FeS_2/g\text{-}C_3N_4$ catalyst. H_2 and CH_3O^- are generated when H^- and CH_3OH react. Moreover, boron in BH_3 interacts with CH_3O^- to form the BH_3 $(CH3O)^-$ ion. Once more, the BH_3 $(OH)^-$ ion is used to transport H_2. In each cycle, the hydrogen adsorption cycle on the catalyst is repeated until the BH_3 $(CH3O)^-$ ion becomes $B(CH_3O)_4$ and H_2 is released

[50-54]. The best catalyst must adsorb large amount of BH_4^- at very short times. Further, the preferred catalyst should increase the volume of hydrogen gas [55].

From the definition of hydrogen generation rate (k), we can estimate the catalytic performance of nanocomposites as a function of H_2 volume (V), mass of the catalyst (m_{cat}) and reaction time (t) [17,56];

$$k = \frac{V}{t.m_{cat}} \qquad (3)$$

The slope of the plots in Fig. 7 were used to compute the rates of hydrogen produced (k). In this case, the obtained data for different Fe_3O_4/FeS_2/g-C_3N_4 nanosheets are given in Fig. 8. Consequently, the rate of hydrogen production for the sample sulfur@g-C_3N_4 was 6333 mL/g.min. While the values of k at 1.0, 2.0 and 3.0 wt% of Fe_3O_4/FeS_2 were 6024, 8464 and 8480 mL/g.min. Now, the sample 3.0 wt% Fe_3O_4/FeS_2 showed the best rate of hydrogen production. This result is related to the structural and surface characteristics of this sample, as it showed a high surface area and a large pore size. Therefore, many active sites were located on the surface of the nanocomposites and induced large amounts of hydrogen.

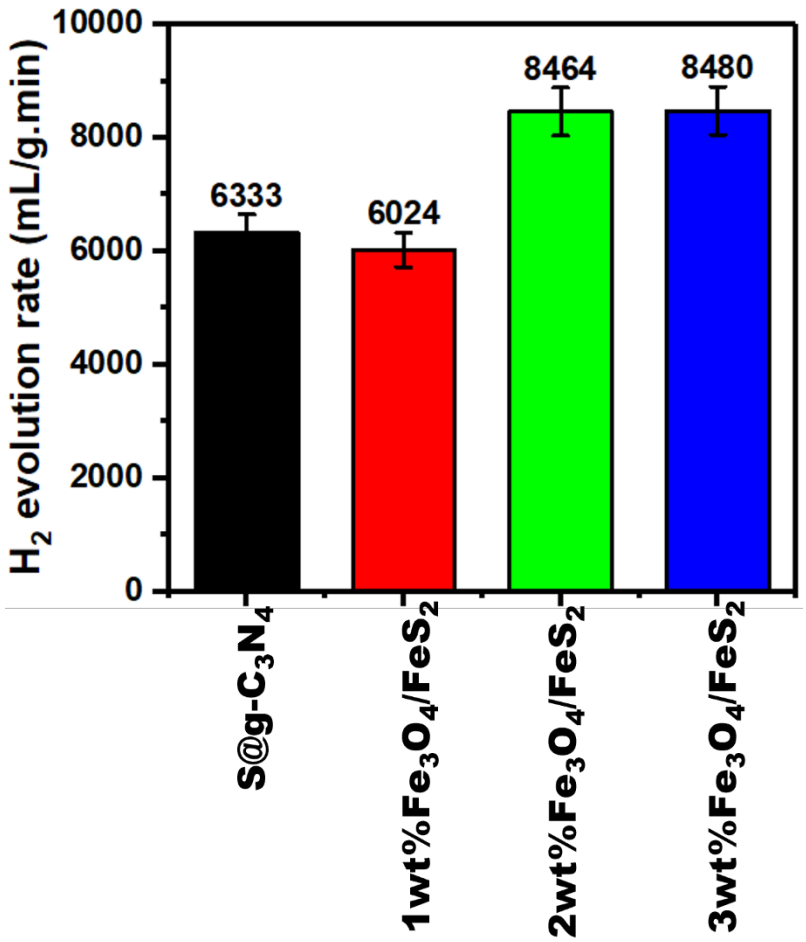

Fig. 8 The rates of H_2 generation at 20 mg of $Fe_3O_4/FeS_2/g\text{-}C_3N_4$ catalyst and 2.5% $NaBH_4$

It is appropriate to make a comparison between the performance of $Fe_3O_4/FeS_2/g\text{-}C_3N_4$ nanocomposites as a catalyst for hydrogen production with their counterparts in the literature. In our previous work, the catalyst of 1.5 wt% $NiS/g\text{-}C_3N_4$ was prepared by polycondensation route and tested for hydrogen production [19]. In that case the rate of hydrogen generation at 293 K was 8654 mL/g.min that is lower than the value reported in the present work. Another study conducted by F. Wang et al [57] used the electroplating technique to synthesize an active catalyst of Ru/NiO-Ni foam. The morphology of the catalyst material was bush-like. Further, this work achieved a rate of production equal to 6000 mL/g.min that is lower than the present finding. On the other hand, the catalytic performance of rutile TiO_2/NH_2 was examined according to the methanolysis hydrolysis of $NaBH_4$ [56]. As a result, the hydrogen production rate in this case reaches 3525 mL/g.min. However, this value is still lower than the estimated value in the present study. Finally, P. Dai et al [58] reported the self-hydrolysis of $NaBH_4$ at the ZIF-67@GO catalyst. The surface

morphology of the composite showed 3D polyhedrons and the rate of H_2 gas production was 3200 mL/g.min. According to these findings, the present 3.0 wt% Fe_3O_4/FeS_2/g-C_3N_4 showed high potential for catalytic production of hydrogen gas.

The efficiency of the Fe_3O_4/FeS_2/g-C_3N_4 catalyst was investigated for 3 cycles. The data were plotted in Fig. 9 and showed a slight decrease in efficiency from 100 to 99.97%. This small decrease may be due to the blocking of surface-active sites for the Fe_3O_4/FeS_2/g-C_3N_4 catalyst after 3.0 cycles.

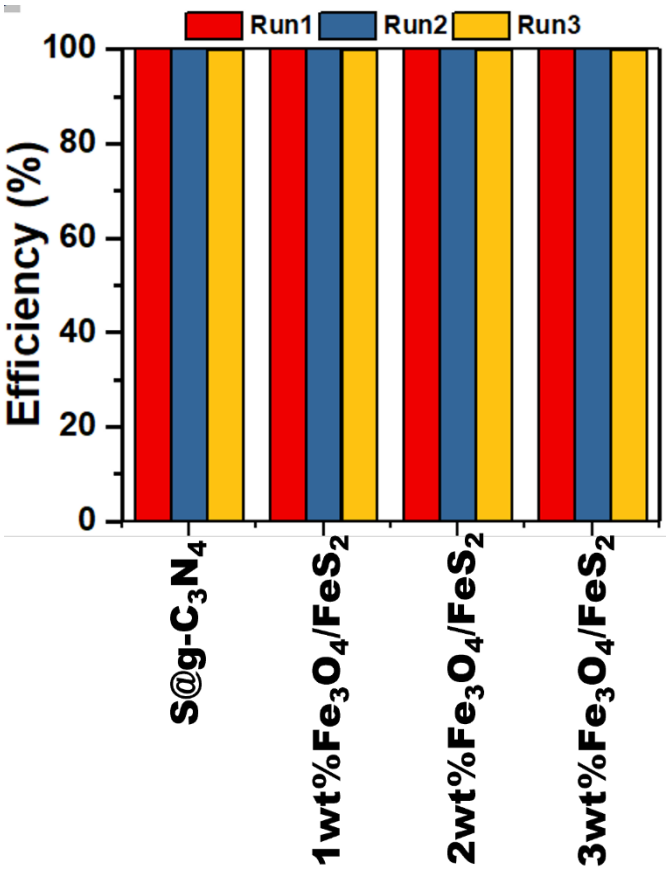

Fig. 9 The reuse experiments of Fe_3O_4/FeS_2/g-C_3N_4 catalysts

Conclusions

Nanocomposites of Fe_3O_4/FeS_2/g-C_3N_4 were developed for catalytic hydrogen generation from sodium borohydride. The XRD diffraction peaks of Fe_3O_4 and FeS_2 cubic phase showed an average crystal size of calculation of 15 and 20 nm. ESEM micrographs showed a 2D broken up sheet structure having more edge sites. The surface area BET of the prepared nanosheets increased from

40 to 162 m^2/g. While the optical energy gap decreased from 2.60 to 2.18 eV. All the samples show an emission peak around 460 nm that related to the transitions of n-π*. The rate of hydrogen production is accelerated as the percentage of Fe_3O_4/FeS_2 increased. The sample 3.0 wt% Fe_3O_4/FeS_2 showed the best rate of hydrogen production with a value of 8480 mL/g.min. Accordingly, the prepared 3.0 wt% Fe_3O_4/FeS_2/g-C_3N_4 nanosheet showed high potential for catalytic production of hydrogen gas.

Acknowledgments

The authors extend their appreciation to the Deputyship for Research & Innovation, Ministry of Education in Saudi Arabia for funding this research work through the project number 223202.

Author's statement: All the authors have contributed in the work, and they are known with the submission.

Declaration of competing interest: The authors declare that they have no known competing financial interests or personal relationships that could have appeared to influence the work reported in this paper.

Data Availability Statement: Data will be made available on reasonable request.

References

1- Shwetharani, R., Sakar, M., Fernando, C. A. N., Binas, V., & Balakrishna, R. G. (2019). Recent advances and strategies to tailor the energy levels, active sites and electron mobility in titania and its doped/composite analogues for hydrogen evolution in sunlight. Catalysis Science & Technology, 9(1), 12-46.
2- Chen, L., Qi, Z., Zhang, S., Su, J., & Somorjai, G. A. (2020). Catalytic hydrogen production from methane: A review on recent progress and prospect. Catalysts, 10(8), 858.
3- Roslan, N. A., Abidin, S. Z., Ideris, A., & Vo, D. V. N. (2020). A review on glycerol reforming processes over Ni-based catalyst for hydrogen and syngas productions. International Journal of Hydrogen Energy, 45(36), 18466-18489.
4- Sohail, M., Anwar, U., Taha, T. A., Qazi, H. I. A., Al-Sehemi, A. G., Ullah, S., ... & Hayat, A. (2022). Nanostructured materials based on g-C3N4 for enhanced photocatalytic activity and potentials application: A review. Arabian Journal of Chemistry, 104070.
5- Hayat, A., Sohail, M., Anwar, U., Taha, T. A., Qazi, H. I. A., Ajmal, Z., ... & Orooji, Y. (2023). A Targeted Review of Current Progress, Challenges and Future Perspective of g-

C3N4 based Hybrid Photocatalyst Toward Multidimensional Applications. The Chemical Record, 23(1), e202200143.
6- Guo, H., Niu, C. G., Yang, Y. Y., Liang, C., Niu, H. Y., Liu, H. Y., ... & Tang, N. (2021). Interfacial Co-N bond bridged CoB/g-C3N4 Schottky junction with modulated charge transfer dynamics for highly efficient photocatalytic Staphylococcus aureus inactivation. Chemical Engineering Journal, 422, 130029.
7- Mahvelati-Shamsabadi, T., Fattahimoghaddam, H., Lee, B. K., Bae, S., & Ryu, J. (2021). Synthesis of hexagonal rosettes of g-C3N4 with boosted charge transfer for the enhanced visible-light photocatalytic hydrogen evolution and hydrogen peroxide production. Journal of Colloid and Interface Science, 597, 345-360.
8- Wan, C., Li, J., Chen, S., Wang, W., & Xu, K. (2021). In situ synthesis and catalytic decomposition mechanism of CuFe2O4/g-C3N4 nanocomposite on AP and RDX. Journal of Analytical and Applied Pyrolysis, 160, 105372.
9- Wang, J., Lian, X., Chen, S., Li, H., & Xu, K. (2022). Effect of Bi2WO6/g-C3N4 composite on the combustion and catalytic decomposition of energetic materials: an efficient catalyst with g-C3N4 carrier. Journal of Colloid and Interface Science, 610, 842-853.
10- Mutalik, C., Lin, I. H., Krisnawati, D. I., Khaerunnisa, S., Khafid, M., Widodo, ... & Kuo, T. R. (2022). Antibacterial Pathways in Transition Metal-Based Nanocomposites: A Mechanistic Overview. International Journal of Nanomedicine, 6821-6842.
11- Mutalik, C., Hsiao, Y. C., Chang, Y. H., Krisnawati, D. I., Alimansur, M., Jazidie, A., ... & Kuo, T. R. (2020). High uv-vis-nir light-induced antibacterial activity by heterostructured TiO2-FeS2 nanocomposites. International journal of nanomedicine, 8911-8920.
12- Kuo, T. R., Liao, H. J., Chen, Y. T., Wei, C. Y., Chang, C. C., Chen, Y. C., ... & Wang, D. Y. (2018). Extended visible to near-infrared harvesting of earth-abundant FeS 2–TiO 2 heterostructures for highly active photocatalytic hydrogen evolution. Green Chemistry, 20(7), 1640-1647.
13- Mutalik, C., Krisnawati, D. I., Patil, S. B., Khafid, M., Atmojo, D. S., Santoso, P., ... & Kuo, T. R. (2021). Phase-dependent MoS2 nanoflowers for light-driven antibacterial application. ACS Sustainable Chemistry & Engineering, 9(23), 7904-7912.
14- Ma, D. N., Li, X. M., Wang, X. Q., & Luo, Y. J. (2021). Preparation of g-C3N4 Nanosheets/CuO with Enhanced Catalytic Activity on the Thermal Decomposition of Ammonium Perchlorate. European Journal of Inorganic Chemistry, 2021(10), 982-988.
15- Liu, X., Ma, R., Zhuang, L., Hu, B., Chen, J., Liu, X., & Wang, X. (2021). Recent developments of doped g-C3N4 photocatalysts for the degradation of organic pollutants. Critical Reviews in Environmental Science and Technology, 51(8), 751-790.
16- Shi, Y., Wang, L., Fu, L., Liu, C., Yu, B., Yang, F., & Hu, Y. (2019). Sodium alginate-templated synthesis of g-C3N4/carbon spheres/Cu ternary nanohybrids for fire safety application. Journal of colloid and interface science, 539, 1-10.
17- Li, P., Miser, D. E., Rabiei, S., Yadav, R. T., & Hajaligol, M. R. (2003). The removal of carbon monoxide by iron oxide nanoparticles. Applied Catalysis B: Environmental, 43(2), 151-162.

18- Saka, C. (2022). Phosphorus decorated g-C3N4-TiO2 particles as efficient metal-free catalysts for hydrogen release by NaBH4 methanolysis. Fuel, 322, 124196.
19- Alshammari, A. H., Alshammari, K., Alotaibi, T., Alshammari, M., Alhassan, S., & Taha, T. A. M. (2023). In Situ Polycondensation Synthesis of NiS-g-C3N4 Nanocomposites for Catalytic Hydrogen Generation from NaBH4. Nanomaterials, 13(5), 938.
20- Ganesan, K., Hayagreevan, C., Rahul, R., Jeevagan, A. J., Adinaveen, T., Bhuvaneshwari, D. S., ... & Amalraj, M. (2022). Catalytic hydrolysis of sodium borohydride for hydrogen production using phosphorylated silica particles. Environmental Science and Pollution Research, 1-14.
21- Saka, C. (2022). Efficient and durable H2 production from NaBH4 methanolysis using N doped hybrid g-C3N4-SiO2 composites with ammonia as a nitrogen source. Fuel, 324, 124594.
22- Alshammari, A. H., Alshammari, M., Alhassan, S., Alshammari, K., Alotaibi, T., & Taha, T. A. M. (2023). MoO3/S@ g-C3N4 Nanocomposite Structures: Synthesis, Characterization, and Hydrogen Catalytic Performance. Nanomaterials, 13(5), 820.
23- Zhang, H., Wei, Q., Wu, G., Qiu, S., Zou, Y., Xia, Y., ... & Chu, H. (2023). Zn-MOF-74-derived graphene nanosheets supporting CoB alloys for promoting hydrolytic dehydrogenation of sodium borohydride. Journal of Alloys and Compounds, 930, 167486.
24- Yan, T., Yan, Q., Wang, X., Liu, H., Li, M., Lu, S., ... & Sun, M. (2015). Facile fabrication of heterostructured gC 3 N 4/Bi 2 MoO 6 microspheres with highly efficient activity under visible light irradiation. Dalton Transactions, 44(4), 1601-1611.
25- Jayaraman, V., Ayappan, C., Vattikondala, G., & Mani, A. (2021). Preparation and characterization of the Cu, Fe co-doped Bi2Ti2O7/EG-g-C3N4 material for organic model pollutants removal under direct sun light irradiation. Materials Research Bulletin, 143, 111439.
26- Li, J., Hao, H., & Zhu, Z. (2016). Construction of g-C3N4-WO3-Bi2WO6 double Z-scheme system with enhanced photoelectrochemical performance. Materials Letters, 168, 180-183.
27- Fang, Y., Fu, X., & Wang, X. (2020). Diverse polymeric carbon nitride-based semiconductors for photocatalysis and variations. ACS Materials Letters, 2(8), 975-980.
28- Liang, Q., Shao, B., Tong, S., Liu, Z., Tang, L., Liu, Y., ... & Peng, Z. (2021). Recent advances of melamine self-assembled graphitic carbon nitride-based materials: design, synthesis and application in energy and environment. Chemical Engineering Journal, 405, 126951.
29- Meng, S., Sun, S., Liu, Y., Lu, Y., & Chen, M. (2022). Synergistic modulation of inverse spinel Fe3O4 by doping with chromium and nitrogen for efficient electrocatalytic water splitting. Journal of Colloid and Interface Science, 624, 433-442.
30- Choi, H., Seo, J. Y., Uhm, Y. R., Sun, G. M., & Kim, C. S. (2021). Crystalline structure and magnetic properties of pyrite FeS2. AIP Advances, 11(1), 015131.
31- Khan, K., Batool, Z., Manzoor, S., Ahmad, D., Aman, S., Alhashmialameer, D., ... & Ashiq, M. N. (2022). Fabrication of substituted Y-type hexaferrites/carbon dots

composites for recording media and photodegradation of dye. Ceramics International, 48(19), 27550-27559.
32- Mahmoud, M. H., Hassan, A. M., Said, A. E. A. A., & Taha, T. A. (2022). Structural, magnetic, and catalytic studies of microwave-combustion/ball-mill synthesized zinc ferrite nanoparticles. Inorganic Chemistry Communications, 144, 109932.
33- Taha, T. A., Saad, R., Zayed, M., Shaban, M., & Ahmed, A. M. (2023). Tuning the surface morphologies of ZnO nanofilms for enhanced sensitivity and selectivity of CO2 gas sensor. Applied Physics A, 129(2), 115.
34- Saka, C. (2021). Sulphur and nitrogen-doped metal-free microalgal carbon catalysts for very active dehydrogenation of sodium borohydride in methanol. International Journal of Hydrogen Energy, 46(35), 18326-18337.
35- Wang, Z. T., Xu, J. L., Zhou, H., & Zhang, X. (2019). Facile synthesis of Zn (II)-doped gC 3 N 4 and their enhanced photocatalytic activity under visible light irradiation. Rare Metals, 38, 459-467.
36- Gao, J., Wang, J., Qian, X., Dong, Y., Xu, H., Song, R., ... & Yao, J. (2015). One-pot synthesis of copper-doped graphitic carbon nitride nanosheet by heating Cu–melamine supramolecular network and its enhanced visible-light-driven photocatalysis. Journal of Solid State Chemistry, 228, 60-64.
37- Fan, C., Miao, J., Xu, G., Liu, J., Lv, J., & Wu, Y. (2017). Graphitic carbon nitride nanosheets obtained by liquid stripping as efficient photocatalysts under visible light. RSC advances, 7(59), 37185-37193.
38- Bojdys, M. J., Müller, J. O., Antonietti, M., & Thomas, A. (2008). Ionothermal synthesis of crystalline, condensed, graphitic carbon nitride. Chemistry–A European Journal, 14(27), 8177-8182.
39- Xia, P., Zhu, B., Yu, J., Cao, S., & Jaroniec, M. (2017). Ultra-thin nanosheet assemblies of graphitic carbon nitride for enhanced photocatalytic CO 2 reduction. Journal of Materials Chemistry A, 5(7), 3230-3238.
40- Wang, A. J., Li, H., Huang, H., Qian, Z. S., & Feng, J. J. (2016). Fluorescent graphene-like carbon nitrides: synthesis, properties and applications. Journal of Materials Chemistry C, 4(35), 8146-8160.
41- Jorge, A. B., Martin, D. J., Dhanoa, M. T., Rahman, A. S., Makwana, N., Tang, J., ... & McMillan, P. F. (2013). H2 and O2 evolution from water half-splitting reactions by graphitic carbon nitride materials. The Journal of Physical Chemistry C, 117(14), 7178-7185.
42- Alshammari, A. H., Alshammari, M., Alshammari, K., Allam, N. K., & Taha, T. A. (2023). PVC/PVP/SrTiO3 polymer blend nanocomposites as potential materials for optoelectronic applications. Results in Physics, 44, 106173.
43- Ahmed, R. M., Taha, T. A., & Ezz-Eldin, F. M. (2021). Investigation of Sm 2 O 3 effect on opto-electrical parameters and dielectric properties of some fluorophosphate glasses. Journal of Materials Science: Materials in Electronics, 32, 28919-28934.
44- Alshammari, A. H., Alshammari, K., Alshammari, M., & Taha, T. A. M. (2023). Structural and Optical Characterization of g-C3N4 Nanosheet Integrated PVC/PVP Polymer Nanocomposites. Polymers, 15(4), 871.

45- Wang, X., Gong, J., Dong, Y., An, S., Zhang, X., & Tian, J. (2022). Energy band engineering of hydroxyethyl group grafted on the edge of 3D g-C3N4 nanotubes for enhanced photocatalytic H2 production. Materials Today Physics, 27, 100806.
46- Song, X., Mao, W., Wu, Y., Wang, M., Liu, X., Zhou, W., & Huo, P. (2022). Fabricating carbon nitride-based 3D/0D intramolecular donor–acceptor catalysts for efficient photoreduction of CO 2. New Journal of Chemistry, 46(42), 20225-20234.
47- Rong, X., Qiu, F., Rong, J., Zhu, X., Yan, J., & Yang, D. (2016). Enhanced visible light photocatalytic activity of W-doped porous g-C3N4 and effect of H2O2. Materials Letters, 164, 127-131.
48- Saka, C., & Balbay, A. (2019). Influence of process parameters on enhanced hydrogen generation via semi-methanolysis and semi-ethanolysis reactions of sodium borohydride using phosphoric acid. International Journal of Hydrogen Energy, 44(57), 30119-30126.
49- Xu, D., Zhang, Y., & Guo, Q. (2021). Research progress on catalysts for hydrogen generation through sodium borohydride alcoholysis. International Journal of Hydrogen Energy, 47(9), 5929-5946.
50- Saka, C. (2023). Metal-free phosphorus and boron-doped graphitic carbon nitride/zeolite hetero-linked particles for highly efficient green hydrogen production in methanol. Environmental Science and Pollution Research, 30, 43480–43495.
51- Saka, C. (2023). Metal-free hybrid composite particles with phosphorus and oxygen-doped graphitic carbon nitride dispersed on kaolin for catalytic activity toward efficient hydrogen release. International Journal of Hydrogen Energy. 48(37), 13864-13876.
52- Saka, C. (2023). Surface modification of graphitic carbon nitride nanoparticles with B, O and S doping/carbon vacancy for efficient dehydrogenation of sodium borohydride in methanol. International Journal of Hydrogen Energy. 48(35), 13123-13138.
53- Saka, C. (2022). Performance of g-C3N4 nanoparticles by EDTA modification and protonation for hydrogen release from sodium borohydride methanolysis. International Journal of Hydrogen Energy, 47(28), 13654-13663.
54- Cafer, S. A. K. A. (2023). Highly active hydrogen generation from sodium borohydride methanolysis and ethylene glycolysis reactions using protonated chitosan-zeolite hybrid metal-free particles. Applied Catalysis B: Environmental, 325, 122335.
55- Demirci, S., Sunol, A. K., & Sahiner, N. (2020). Catalytic activity of amine functionalized titanium dioxide nanoparticles in methanolysis of sodium borohydride for hydrogen generation. Applied Catalysis B: Environmental, 261, 118242.
56- Saka, C. (2022). g-C3N4 particles with boron and oxygen dopants/carbon vacancies for efficient dehydrogenation in sodium borohydride methanolysis. International Journal of Hydrogen Energy, 47(44), 19016-19026.
57- Wang, F., Luo, Y., Zhang, Y., Wang, Y., & Zhu, H. (2020). Preparation of bush-like Ru/NiO-Ni foam catalyst and its performance in hydrogen production from sodium borohydride alcoholysis. Energy & Fuels, 34(9), 11365-11372.
58- Dai, P., Yao, Y., Hu, E., Xu, D., Li, Z., & Wang, C. (2021). Self-assembled ZIF-67@ graphene oxide as a cobalt-based catalyst precursor with enhanced catalytic activity toward methanolysis of sodium borohydride. Applied Surface Science, 546, 149128.